Video Article

Ohmic Contact Fabrication Using a Focused-ion Beam Technique and Electrical Characterization for Layer Semiconductor Nanostructures

Ruei-San Chen[1], Chih-Che Tang[2], Wei-Chu Shen[2], Ying-Sheng Huang[2]

[1]Graduate Institute of Applied Science and Technology, National Taiwan University of Science and Technology

[2]Department of Electronic Engineering, National Taiwan University of Science and Technology

Correspondence to: Ruei-San Chen at rsc@mail.ntust.edu.tw

URL: https://www.jove.com/video/53200
DOI: doi:10.3791/53200

Keywords: Engineering, Issue 106, focused-ion beam (FIB), ohmic contact, layer semiconductor, molybdenum diselenide ($MoSe_2$), molybdenum disulphide (MoS_2), electrical conductivity, atomic force microscopy (AFM), high-resolution transmission electron microscopy (HRTEM), selected-area electron diffractometry (SAED), energy-dispersive X-ray spectroscopy (EDX)

Date Published: 12/5/2015

Citation: Chen, R.S., Tang, C.C., Shen, W.C., Huang, Y.S. Ohmic Contact Fabrication Using a Focused-ion Beam Technique and Electrical Characterization for Layer Semiconductor Nanostructures. *J. Vis. Exp.* (106), e53200, doi:10.3791/53200 (2015).

Abstract

Layer semiconductors with easily processed two-dimensional (2D) structures exhibit indirect-to-direct bandgap transitions and superior transistor performance, which suggest a new direction for the development of next-generation ultrathin and flexible photonic and electronic devices. Enhanced luminescence quantum efficiency has been widely observed in these atomically thin 2D crystals. However, dimension effects beyond quantum confinement thicknesses or even at the micrometer scale are not expected and have rarely been observed. In this study, molybdenum diselenide ($MoSe_2$) layer crystals with a thickness range of 6-2,700 nm were fabricated as two- or four-terminal devices. Ohmic contact formation was successfully achieved by the focused-ion beam (FIB) deposition method using platinum (Pt) as a contact metal. Layer crystals with various thicknesses were prepared through simple mechanical exfoliation by using dicing tape. Current-voltage curve measurements were performed to determine the conductivity value of the layer nanocrystals. In addition, high-resolution transmission electron microscopy, selected-area electron diffractometry, and energy-dispersive X-ray spectroscopy were used to characterize the interface of the metal–semiconductor contact of the FIB-fabricated $MoSe_2$ devices. After applying the approaches, the substantial thickness-dependent electrical conductivity in a wide thickness range for the $MoSe_2$-layer semiconductor was observed. The conductivity increased by over two orders of magnitude from 4.6 to 1,500 Ω^{-1} cm^{-1}, with a decrease in the thickness from 2,700 to 6 nm. In addition, the temperature-dependent conductivity indicated that the thin $MoSe_2$ multilayers exhibited considerably weak semiconducting behavior with activation energies of 3.5-8.5 meV, which are considerably smaller than those (36-38 meV) of the bulk. Probable surface-dominant transport properties and the presence of a high surface electron concentration in $MoSe_2$ are proposed. Similar results can be obtained for other layer semiconductor materials such as MoS_2 and WS_2.

Video Link

The video component of this article can be found at https://www.jove.com/video/53200/

Introduction

Transition metal dichalcogenides (TMDs), such as MoS_2, $MoSe_2$, WS_2, and WSe_2, have an interesting two-dimensional (2D) layer structure and semiconducting properties[1-3]. Scientists have recently discovered that the monolayer structure of MoS_2 shows a substantially enhanced light-emitting efficiency because of the quantum confinement effect. The finding of the new direct-bandgap semiconductor material has attracted substantial attention[4-7]. In addition, the easily stripped layer structure of TMDs is an excellent platform for studying the fundamental properties of 2D materials. Unlike metallic graphene without the bandgap, TMDs have inherent semiconducting characteristics and have a bandgap in the range of 1-2 eV[1,3,8]. The 2D structures of the ternary compounds of TMDs[9] and the possibility of the integration of these compounds with graphene provide an unprecedented opportunity to develop ultrathin and flexible electronic devices.

Unlike graphene, the room temperature electron mobility values of 2D TMDs are at a moderate level (1-200 $cm^2V^{-1}sec^{-1}$ for MoS_2[10-17]; approximately 50 $cm^2V^{-1}sec^{-1}$ for $MoSe_2$[18]). The optimal mobility values of graphene have been reported to be higher than 10,000 $cm^2V^{-1}sec^{-1}$.[19-21] Nevertheless, semiconducting TMD monolayers exhibit excellent device performance. For instance, the MoS_2 and $MoSe_2$ monolayers or multilayer field-effect transistors exhibit extremely high on/off ratios, up to 10^6-10^9 [10,12,17,18,22]. Therefore, it is crucial to understand the fundamental electrical properties of the 2D TMDs and their bulk materials.

However, studies of the electrical properties of the layer materials have been partially hampered because of the difficulty in forming good ohmic contact on the layer crystals. Three approaches, shadow mask deposition (SMD)[23], electron beam lithography (EBL)[24,25], and focused-ion beam (FIB) deposition,[26,27] have been used to form electrical contacts on nanomaterials. Because SMD typically involves the use of a copper grid as the mask, the spacing between two contact electrodes is mostly larger than 10 μm. Unlike EBL and FIB deposition, metal deposition of electrode arrays on a substrate is performed without targeting or selecting nanomaterials of interest in the SMD method. This approach cannot guarantee that the metal patterns are correctly deposited on individual nanomaterials as the electrodes. The result of the SMD method has an element of chance. The EBL and FIB deposition methods are used in the scanning electron microscope (SEM) system; nanomaterials can be directly

observed and selected for electrode deposition. In addition, EBL can be used to easily fabricate metal electrodes with a line width and a contact electrode spacing smaller than 100 nm. However, the residual resist on the nanomaterial surface left during lithography inevitably results in the formation of an insulating layer between the metal electrode and the nanomaterial. Thus, EBL leads to high contact resistance.

The main advantage of electrode fabrication through FIB deposition is that it leads to low contact resistance. Because metal deposition is performed by the decomposition of an organometallic precursor by using an ion beam at the defined area, metal deposition and ion bombardment occur simultaneously. This could destroy the metal–semiconductor interface and prevent the formation of Schottky contact. Ion bombardment can also eliminate surface contaminants such as hydrocarbons and native oxides, which decreases contact resistance. Ohmic contact fabrication through FIB deposition has been demonstrated for different nanomaterials[27-29]. In addition, the entire fabrication procedure in the FIB deposition approach is simpler than that in EBL.

As layer semiconductors typically show highly anisotropic electrical conduction, the conductivity in the layer-to-layer direction is several orders of magnitude lower than that in the in-plane direction[30,31]. This characteristic increases the difficulty of fabricating ohmic contacts and determining electrical conductivity. Therefore, in this study, FIB deposition was used for studying the electrical properties of layer semiconductor nanostructures.

Protocol

1. Structural Characterization of $MoSe_2$ Layer Crystals (See Step 1 in Figure 1)

1. XRD Measurement Procedure
    1. Mount a $MoSe_2$ layer crystal (with the size range of 5 x 5 x 0.1-10 x 10 x 0.5 mm^3) or crystal powder (which was mixed with quartz powder and binder and was smeared on the slide glass) on the holder.
    2. Press the holder by a slide glass to ensure layer crystal surface parallel to the holder surface.
    3. Load the sample holder into the diffractometer.
    4. Close the doors of diffractometer.
    5. Calibrate beam line accordingly to manufacturer's instructions.
    6. Input measurement parameters such as the 2 scan range (10-80°), the increment (0.004°), and the dwell time (0.1 sec).
    7. Start the DIFFRAC.Measurement Center program on the computer attached to the diffractometer and then save data and name data file according to manufacturer's protocol.
    8. Analyze the XRD pattern by identifying the positions of the diffraction peaks using the software and then compare with the standard data from JCPDS card database to confirm the single out-of-plane orientation and single-crystalline quality of the $MoSe_2$ layer crystals[32,33].

2. Micro-Raman Measurement Procedure
    1. Perform the Raman equipment calibration using a silicon wafer as the standard sample. The measurement of the silicon wafer is the same as the procedure described below for the interested $MoSe_2$ layer crystal.
    2. Mount a $MoSe_2$ layer crystal on the slide glass.
    3. Load the slide glass on the holder of optical microscope and focus the sample surface with a white light source.
    4. Switch the light source from a white light to a laser beam (wavelength at 514 nm).
    5. Input measurement parameters such as the wavenumber scan range (150-500 cm^{-1}), the integration time (10 sec), and the number of scan times (10-30 times).
    6. Start the program on computer attached to the Raman spectrometer and then save data and name data file according to manufacturer's protocol.
    7. Analyze the Raman spectrum by identifying their peak widths and positions using the software and then compare with standard data from references to confirm the crystalline structure type and quality of the $MoSe_2$ layer crystals[34,35].

2. Fabrication of $MoSe_2$ Layer Nanocrystal Devices

1. Mechanical Exfoliation of Layer Crystals
    1. Clean tweezers with acetone and alcohol.
    2. Pick the $MoSe_2$ layer crystals (4 to 8 pieces) with a shiny surface (*i.e.* mirror-like crystal face) and an area size larger than 0.5 x 0.5 mm^2 with the tweezers and put them on the dicing tape with an area size of 20 x 60 mm^2.
    3. Fold the tape in half to exfoliate the layer crystal and repeat the action approximately twenty times. Usually layer crystals can be stripped into many micrometer-sized crystals in width (see Step 2 in **Figure 1**).
    4. Load the dicing tape with the layer nanocrystal powder into the SEM chamber to observe the sizes and morphologies of these stripped $MoSe_2$ layer microcrystal. If the width distributions of the layer nanocrystal are at 1-20 μm, the nanocrystal powder can meet the criteria for the device fabrication.

2. Dispersion of the Layer Nanocrystals on the Device Template
    1. Place the dicing tape with the layer nanocrystal powder upside-down on the device template. The template is SiO_2 (300 nm)-coated silicon substrate with sixteen pre-patterned Ti (30 nm)/Au (90 nm) electrodes on the SiO_2 surface (see Step 4 in **Figure 1**). The area size of the template is 5 x 5 mm^2.
    2. Tap the dicing tape lightly to make some nanocrystals (roughly 10 to 100 pieces) fall on the template.
    3. Check the number density and dispersion condition of the nanocrystal on the template by optical microscope or sometimes by SEM if the dispersed nanocrystals can be not observed by optical microscope. Usually 2 to 5 pieces of nanocrystals (area size larger than

2 x 2 μm^2) dispersed on the center square (with area of 80 x 80 μm^2) of the template without overlapping to each other are the better condition for the next FIB processing.

3. Electrode Fabrication by FIB
    1. Mount templates on the FIB holder using conducting copper foil tape. Typically, the area of conducting tape of 3 x 2.4 cm^2 was required for mounting 6-8 templates.
    2. Load the holder into the FIB chamber.
    3. Evacuate the chamber to the vacuum degree down to 10^{-5} mbar by clicking the button “Pump”.
    4. Set the electron beam current (41 pA) and acceleration voltage (10 kV) for the SEM mode.
    5. Set the ion beam current (0.1 nA) and acceleration voltage (30 kV) for the FIB mode.
    6. Warm up the ion beam system and gas-injection-system (GIS) by clicking the button “beam on” and the button “Cold” in the “Gas Injection” block, respectively.
    7. Turn on the electron-beam by clicking the button “Beam On” and focus the image at a low magnification of 100X.
    8. Set the z-axial working distance (WD) at 10 mm for SEM mode.
    9. Set the magnification at 5,000X and focus.
    10. Set the tilt angle of the holder to 52 degrees by clicking the button “Navigation” and input the tilt angle “52”.
    11. Select a $MoSe_2$ layer nanocrystal with a certain thickness (ranging from 5 to 3,000 nm) and a rectangular and square shape for the electrode fabrication.
    12. Take the SEM images at different magnifications (from 1,000X to 10,000X) of the targeted pristine material before electrode fabrication by clicking the button “Snapshot”.
    13. Switch to FIB mode and take an FIB image by the snapshot mode to reduce the exposure time of the targeted material under ion beam bombardment.
    14. Define the electrode deposition area, select the “Pt deposition” mode, and input the thickness (0.2-1.0 μm) value of the deposited Pt electrode.
    15. Introduce the capillary of GIS into the chamber by clicking the box “Pt dep” in the “Gas Injection” block.
    16. Take an image by the snapshot mode again and modify the position of the electrodes if the originally defined pattern shifts slightly.
    17. Turn on the FIB deposition by clicking the button “Start Patterning”.
    18. After deposition, draw the capillary of GIS back by unclicking the box “Pt dep” in the “Gas Injection” block.
    19. Switch to SEM mode and check the result of the deposited Pt electrodes on the layer nanocrystal.
    20. Take the SEM images at different magnifications of the completed devices with two or four electrodes (see Step 3 in **Figure 1**).
    21. Set the tilt angle of the holder return to 0 degrees by clicking the button “Navigation” and input the tilt angle “0”.
    22. Take the top-viewed SEM images at different magnifications for the estimations of the material width and electrode inter-distance by clicking the button “Snapshot”.
    23. Turn off the electron-beam and ion beam systems and cool down GIS system by clicking the button “Beam Off” and the button “Warm” in the “Gas Injection” block, respectively.
    24. Vent the chamber by introducing nitrogen gas by clicking the buttons “Vent” and then take the holder out of the chamber. It typically takes 5 to 10 min to finish the venting process.
    25. Close the chamber door and evacuate the chamber.

3. Characterizations of the $MoSe_2$ Layer Nanocrystal Devices

1. Thickness Measurement of the Layer Nanocrystals by AFM
    1. Install the AFM cantilever to the probe holder.
    2. Turn on AFM program and select “ScanAsyst” mode.
    3. Load the probe holder and connect it with the laser diode head of AFM station.
    4. Perform the calibration to align the incident laser beam position and the cantilever according to manufacturer’s protocol.
    5. Mount the sample (the template chip with FIB-fabricated layer nanocrystal devices) on the sample holder by Cu foil tape.
    6. Load the sample holder to the AFM station.
    7. Move the sample holder to the position approximately underneath the laser beam or AFM cantilever.
    8. Lower down AFM cantilever to the focus position by focusing the optical microscope image of the layer nanocrystal.
    9. Input scan parameters such as the scan area (6 x 6-30 x 30 μm^2), the frequency (0.5-1.5 Hz), and the resolution (256-512 lines).
    10. Start the program and save data according to the manufacturer’s protocol.
    11. Raise the AFM cantilever and take the sample holder out.
    12. Load the second sample and repeat the measurement procedure described above if need.
    13. Estimate the thickness of layer nanocrystals by analyzing the AFM image and height profile using the software “NanoScope Analysis”. Select a lateral height profile from the AFM image and determine the average thickness value by the flatten area of the profile. (See **Figure 2d** and **2e**)

2. Current versus voltage (*I*-*V*) measurement of the layer nanocrystals
    1. Mount the sample (the template chip with FIB-fabricated layer nanocrystal devices) on the mica substrate by Cu foil tape.
    2. Bond the enameled wires or Cu wires on the electrodes of the chip by Ag paste. (See Step 4 in **Figure 1**.)
    3. Load the completed sample in the probe station chamber and fix it on the sample holder by Cu foil tape. The cryogenic probe station was located in the dark environment. (See Step 5 in **Figure 1**.)
    4. Solder the electrical wires of the sample and the metal electrodes of the probes one by one.
    5. Cap the chamber top and evacuate the chamber down to 10^{-4} mbar. Cool down sample to the 77 K by introducing liquid nitrogen into the probe station. Set the temperature range (usually from 80 to 320 K), interval, and dwell time for the temperature control. (Necessary only for temperature-dependent measurement).

6. Set the applied voltage sweeping range (typically from -1 to 1 V), voltage interval (0.01 V), and the limited maximal current (10 or 100 μA) in an ultrahigh-impedance multifunctional electrometer for the two-terminal *I-V* measurement. For four-terminal measurement, set the applied current sweeping range (typically from -100 to 100 μA) and current interval (1 μA).
7. Start the program and save the *I-V* data at room temperature or at different temperatures.
8. Open the chamber cap if necessary and take the sample out of the chamber.
9. Load the second sample if need and repeat the procedure described above.
10. Analyze the *I-V* curve by plotting the measured current versus applied voltage data using the software. Fit the *I-V* curve by selecting the Linear Fitting function. Check the linearity of the *I-V* curve and obtain the slope value (*i.e.* conductance value). (See Step 6 in **Figure 1**.)
11. Repeat the Step 3.2.10 for the *I-V* curves measured at different temperatures if need.
12. Calculate the conductivity (σ) value according to the equation $\sigma = G(t/tw)$ by adopting the parameters obtained by *I-V*, SEM, and AFM measurements including conductance (G), thickness (t), width (w) and length (l) of the layer nanocrystal.
13. Plot the curves of the conductance and conductivity values versus thickness of layer nanocrystals.

Representative Results

The determined values of the electrical conductance (G) and conductivity (σ) of layer nanomaterials with different thicknesses are highly dependent on the quality of the electrical contacts. The ohmic contacts of the FIB-deposition-fabricated two-terminal $MoSe_2$ devices are characterized by measuring the current–voltage (*I–V*) curve. The room temperature *I–V* curves for the two-terminal $MoSe_2$ nanoflake devices with different thicknesses are shown in **Figure 2a**. The *I–V* curves follow a linear relationship. This confirms the ohmic contact condition of the $MoSe_2$ devices.

Partial devices with four electrodes were fabricated to further rule out the potential effect of the contact resistance. **Figure 2b** illustrates the typical *I–V* curves measured by two-electrode and four-electrode methods at room temperature for the same nanoflake with a thickness at 33 nm. The calculated σ values for the two-probe and four-probe measurements are at 117 and 118 $\Omega^{-1}cm^{-1}$, respectively. Because the σ values calculated using two-probe and four-probe measurements for the same devices were highly similar, the influence of contact resistance on the determined G and σ values in this study was negligible. **Figures 2c** and **2d** illustrate the representative field-emission scanning electron microscope (FESEM) images of the two-terminal and four-terminal $MoSe_2$ devices, respectively. The thicknesses of the $MoSe_2$ nanoflakes on the devices were estimated using atomic force microscopy (AFM) measurements; a sample measurement is shown in **Figures 2e** and **2f**.

The metal–semiconductor interface of the electrical contact in the $MoSe_2$ devices was further examined using high-resolution transmission electron microscopy (HRTEM), selected-area electron diffractometry (SAED), and energy-dispersive X-ray spectroscopy (EDX). **Figure 3a** shows the cross-sectional transmission electron microscopy (TEM) image of the Pt/$MoSe_2$ interface. The image shows that an alloy layer (25-30 nm) was formed between Pt and $MoSe_2$ because of ion beam bombardment. HRTEM images of the alloy/$MoSe_2$ interface (spot 4, **Figure 3b**) and the $MoSe_2$ region (spot 3, **Figure 3c**) show an amorphous alloy formed at the surface of single-crystal $MoSe_2$.

The EDX spectrum and the ring pattern of SAED in **Figure 3d** show that Pt is the main constituent and that the metal electrode has a polycrystalline structure. Similar measurements, shown in **Figure 3e**, indicated an ion-bombarded alloy with an amorphous-like structure and containing a mixture of Mo, Se, and Pt at a ratio of 2:4:1. The single-crystal $MoSe_2$ nanoflake was further confirmed by the EDX and SAED measurements, which are shown in **Figure 3f**.

For the ohmic contact fabricated using the FIB deposition method, in $MoSe_2$ multilayer nanostructures with different thicknesses, the G and σ values can be precisely determined. **Figure 4a** shows the statistic G values for the $MoSe_2$ nanoflakes with different thicknesses. It can be observed that the G value does not show an observable change or a change in the thickness over two orders of magnitude. This observation is opposite to theoretical predictions, according to which G is linearly dependent on the thickness (t) for a uniform current flow and is written as

$$G = \frac{I}{V} = \sigma\frac{A}{l} = \sigma\frac{wt}{l}, (1),$$

Where A is the area for current transport, and l, w, and t are the length, width, and thickness of the conductor, respectively.

The σ value can be obtained using Equation (1). **Figure 4b** shows the conductivity as a function of the thickness (σ–t). The value of σ increases by over two orders of magnitude, from 4.6 to 1,500 $\Omega^{-1}cm^{-1}$ when t decreases from 2,700 to 6 nm. An inverse power-law $\sigma \propto t^{-\beta}$ is obtained, where the fitted β value is 0.93. The σ values (0.1-1 $\Omega^{-1}cm^{-1}$)[36-38] for the thickness in the bulk region (t: 10-100 μm) are also located on the fitted line.

In principle, σ is an intrinsic property without any dimension effects. The strong thickness dependence of σ implies that current conduction mainly occurs at the surface of the $MoSe_2$ layer material. If the surface conduction path is several orders of magnitude higher than the bulk, the G value does not increase and becomes a constant, even if the thickness increases.

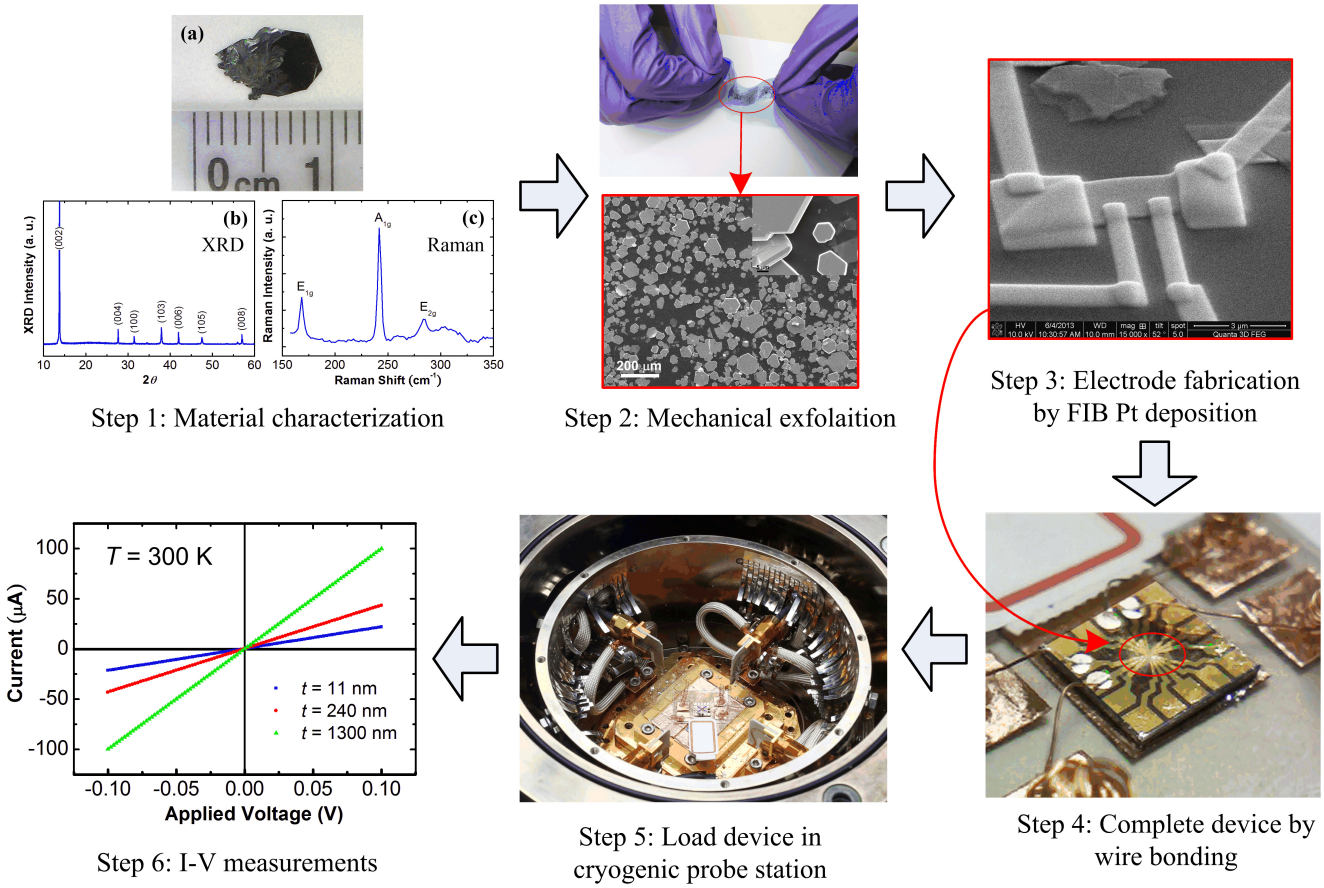

Figure 1: Procedure for device fabrication and electrical characterization of $MoSe_2$ nanoflakes. Step 1: Morphological and structural characterizations of $MoSe_2$ bulk layer crystals by XRD and Raman spectroscopy. Step 2: Mechanical exfoliation of bulk layer crystals by dicing tape and observe the morphology of stripped flakes by FESEM. Step 3: Electrode fabrication of nanoflakes by FIB Pt deposition. Step 4: Complete the device by mounting the sample chip on mica substrate and bonding enameled wire on the electrodes of the chip by Ag paste. Step 5: Load sample in the cryogenic probe station. Step 6: Perform *I-V* measurement and analyze the data.

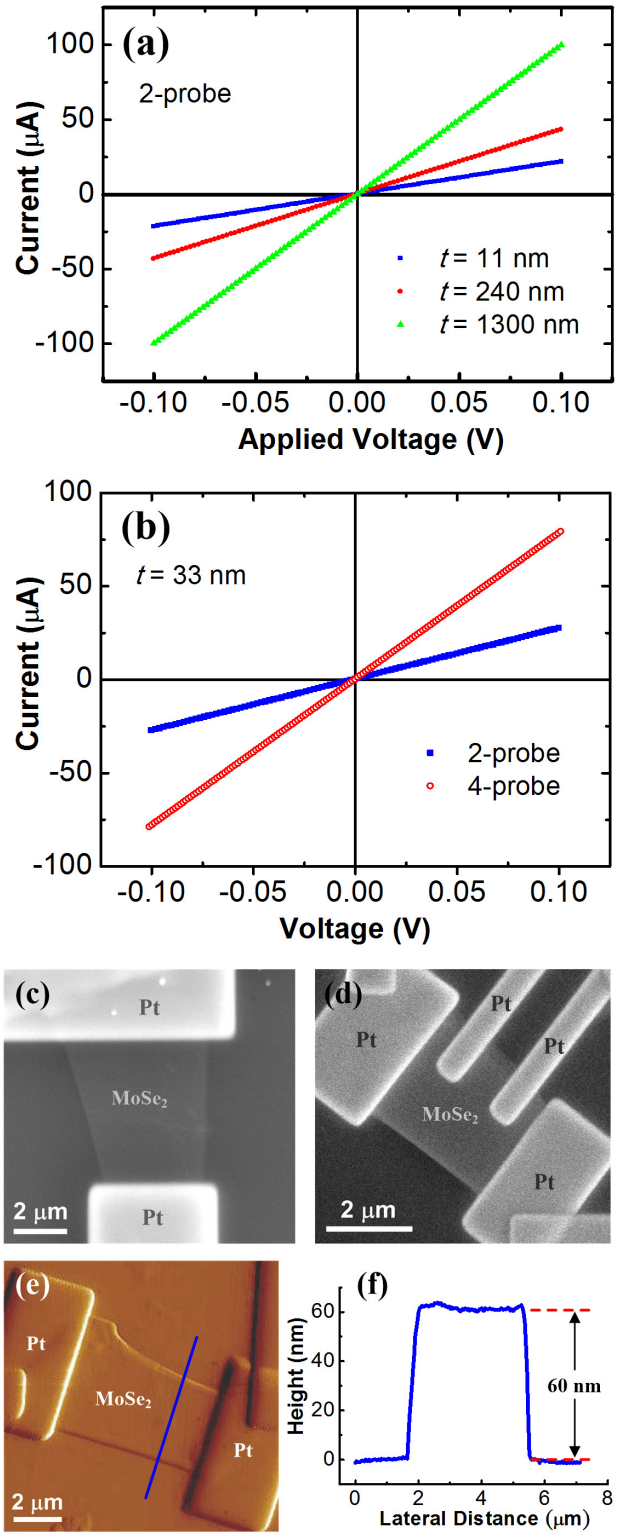

Figure 2: *I-V* curve, FESEM, and AFM measurements for two- and four- terminal $MoSe_2$ nanoflake devices. (**a**) The *I-V* curves measured by the two-probe method at room temperature for the $MoSe_2$ nanoflakes with different thicknesses at 11, 240, and 1,300 nm. (**b**) The *I-V* curves measured by the two-probe and four-probe methods at room temperature for a $MoSe_2$ nanoflake with a thickness at 33 nm. The representative FESEM images of (**c**) the two-terminal and (**d**) the four-terminal $MoSe_2$ devices fabricated by FIB approach. (**e**) A typical AFM image and (**f**) its cross-sectional height profile along the blue line in (**e**) for a $MoSe_2$ device with the thickness at ~60 nm. (Reprinted with permission from Ref. 28, Copyright @ The IOP Publishing Ltd.)

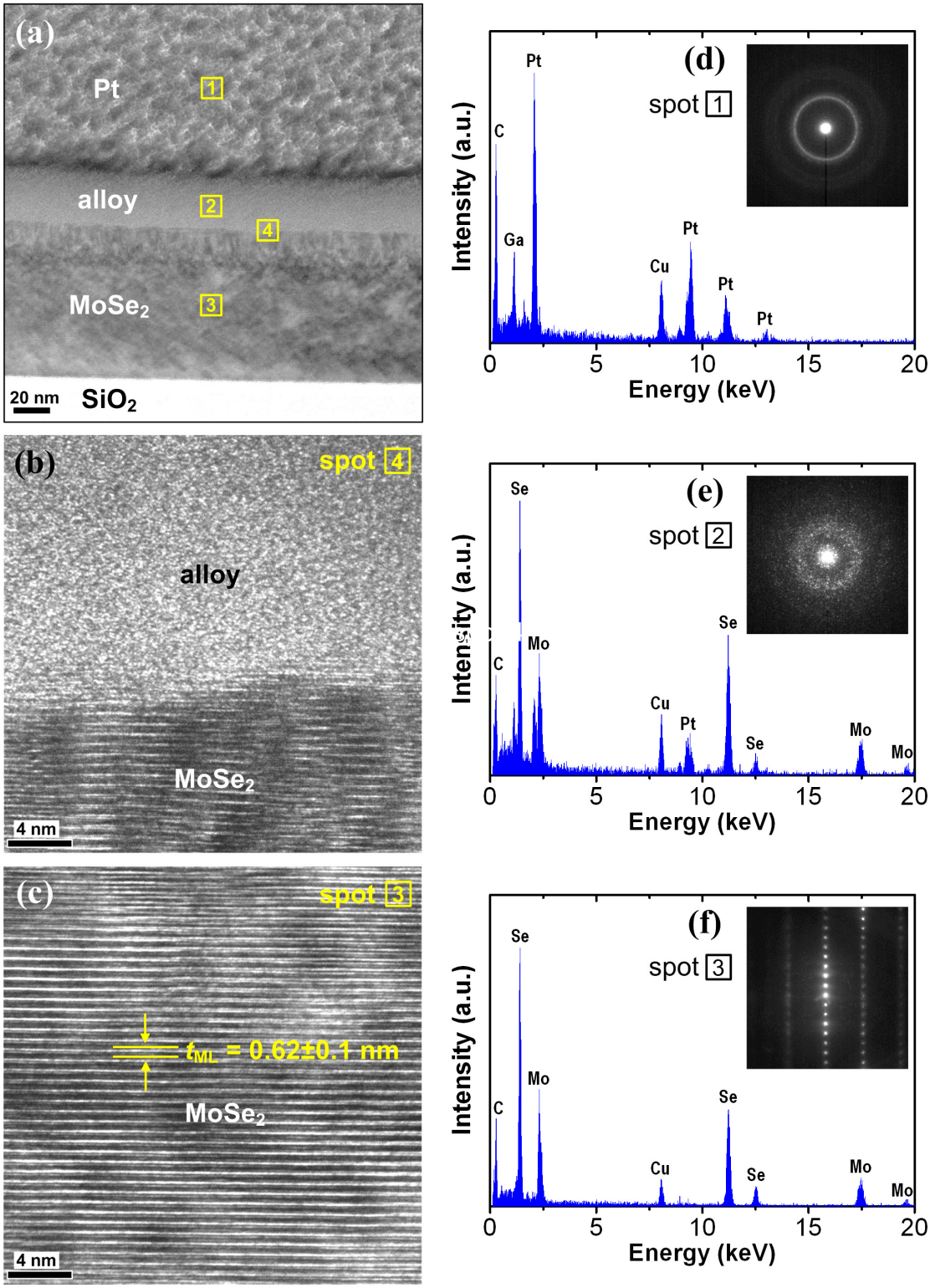

Figure 3: HRTEM, SAED, and EDX analyses for the Pt/$MoSe_2$ interface in the device. (**a**) The cross-sectional TEM image of the Pt metal/$MoSe_2$ semiconductor interface in the $MoSe_2$ nanoflake device (*t* ~110 nm) fabricated by FIB approach. The numeric labels indicate the different probing regions for HRTEM, SAED, and EDX analyses. 1: Pt metal electrode, 2: ion-bombarded alloy region, 3: $MoSe_2$ multilayer, and 4: alloy/$MoSe_2$ interface. The HRTEM image of (**b**) the alloy/$MoSe_2$ interface (spot 4) and (**c**) the $MoSe_2$ region (spot 3). The EDX spectra and the corresponding SAED patterns for (**d**) the Pt electrode (spot 1), (**e**) the alloy region (spot 2), and (**f**) the $MoSe_2$ nanoflake (spot 3), respectively. (Reprinted with permission from Ref. 28, Copyright @ The IOP Publishing Ltd.)

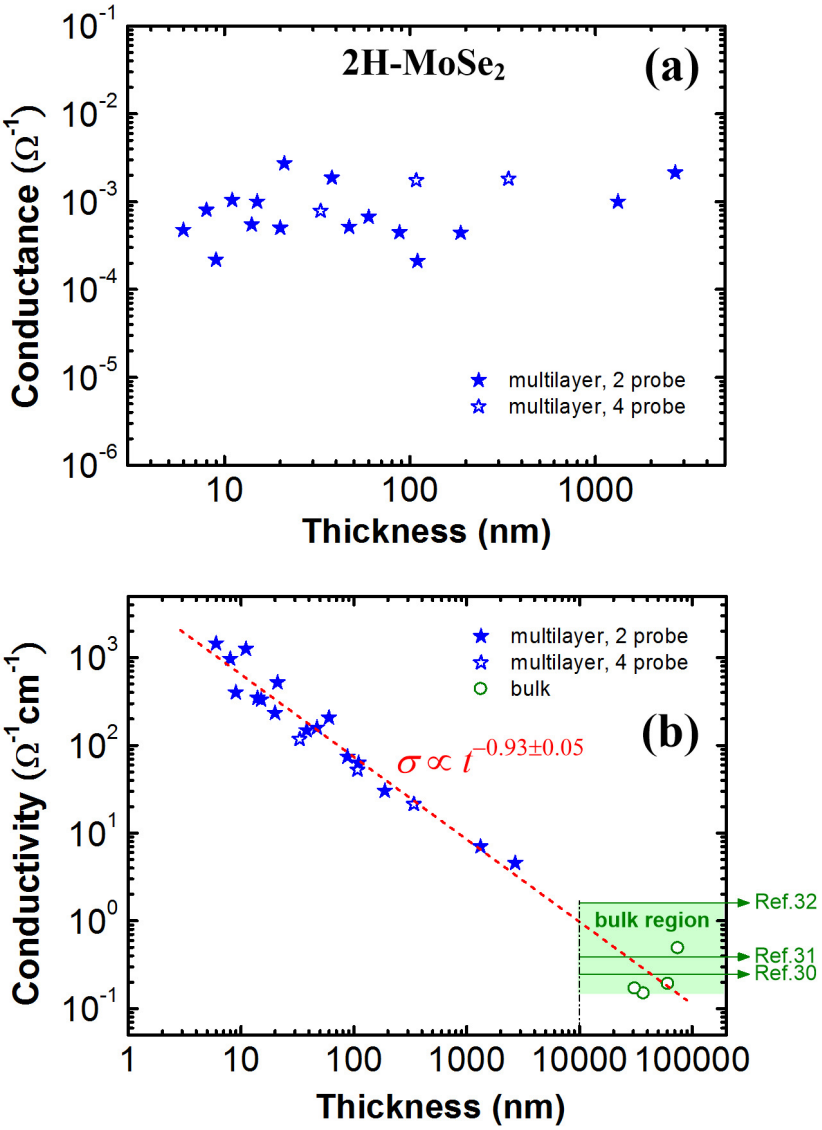

Figure 4: Thickness-dependent conductivity in $MoSe_2$ nanoflakes. (**a**) The electrical conductance and (**b**) the log-log plot of the electrical conductivity values for the $MoSe_2$ nanoflake with different thicknesses ranged from 6 to 2,700 nm measured by two-probe (blue solid star) and four-probe (blue open star) methods. The conductivity values of the $MoSe_2$ bulk crystals obtained by our measurements (green open circle) and from the references are also plotted for comparison. The $MoSe_2$ bulks without the thickness information in the Refs. 32, 33, 34 are assumed to be higher than 10 μm and their conductivity levels are represented by green arrows. The red dash line is the fitting line for the conductivity versus thickness data of the $MoSe_2$ nanoflakes. (Reprinted with permission from Ref. 28, Copyright @ The IOP Publishing Ltd.)

Discussion

The accurate determination of the σ value and its dimension dependence in the layer nanocrystals is highly dependent on the quality of the electrical contacts. The FIB deposition method used for metal electrode deposition played a crucial role throughout the study. According to electrical, structural, and composition analyses, the fabrication of stable and highly reproducible ohmic contacts, using FIB deposition method, in the $MoSe_2$ or MoS_2 devices was facilitated by the formation of the amorphous conductive alloy between the Pt metal and $MoSe_2$ layer semiconductor. The defective alloy structure at the $MoSe_2$ surface that shows a high carrier density could effectively minimize the effect of Schottky contact. The surface contaminants of semiconductors, such as native oxides and hydrocarbons, which are generally considered to originate from the insulating layer between the metal and the semiconductor contacts, can be eliminated by ion beam bombardment. The elimination can explain the low contact resistance in the FIB-deposition-fabricated layer crystal devices.

Although the experimental FIB deposition method provides reliable ohmic contacts for the electrode fabrication of layer semiconductor nanostructures, the minimal spacing between the metal electrodes was limited. It was controlled to be above 1 μm in this study. The main reason for the limitation is that the FIB-deposited metal electrode does not have clear edges and sharp side walls because of the Gaussian distribution

of the ion beam flux in the radial direction. The lack of clear edges and sharp sidewalls can result in material surface contamination and an electrical short circuit if two electrodes are deposited too close to each other (typically closer than 500 nm).

In addition, material processing in the ion beam environment inevitably damages the material surface, leading to a change in the inherent material properties. To avoid potential damage to the material surface by the ion beam during FIB deposition, we attempted to minimize the ion beam exposure time. Typically, most of the steps of the procedure (including selecting suitable nanocrystals, mapping the position, and recording images) were initially performed in the SEM mode; subsequently, the mode was switched to the FIB mode. Therefore, the sample surface was exposed to the ion beam for a considerably short time (in the snapshot mode), which corresponded to the time taken for operating at FIB mode for identifying the Pt deposited areas. Furthermore, surface protection can be provided by coating an insulating organic material (such as bathocuproine) on the layer nanocrystal prior to FIB deposition (not mentioned in the protocol).

EBL, which is the most widely used method, can provide a much smaller spacing between electrodes (shorter than 100 nm) compared with FIB deposition. Potential damage to the studied materials can be prevented by using EBL. However, EBL requires the use of a resist. Because the complete removal of the resist coated on the material surface is difficult, the residual resist can result in high contact resistance between the contact metal and the studied material. This problem reduces the yield of ohmic contacts considerably and hampers the use of EBL as a microelectrode fabrication method. Therefore, FIB technique can be a good choice for microelectrode fabrication with reliable and reproducible ohmic contact in addition to EBL.

However, in this study, the minimal thickness of $MoSe_2$ layer material only reaches 6 nm (approximately 9-10 monolayers). The electrical contact quality for the ultrathin layer materials with thickness lower than 5 monolayers is still unknown. It is expected that the contact area in the ultrathin layer materials may be totally alloyed because the Pt-Mo-Se alloy thickness (25-30 nm) induced by the ion bombardment is higher than the material thickness. Further work is still required to elaborate the alloy effect on the ohmic contact property using FIB approach.

In reality, the FIB deposition method was developed mainly for material milling or etching on micrometer and nanometer scales. Metal deposition is only an extended use of the method for coating or protecting material surfaces. However, in this report, the FIB deposition method was adopted for ohmic contact fabrication in layer semiconductor nanostructures. The observation of the thickness effect on the transport properties in these 2D nanomaterials was facilitated by the use of the FIB deposition method. Electrode fabrication at the micrometer or submicrometer scale with reliable ohmic contact quality has been a challenge and is crucial for a variety of applications, such as fundamental electrical characterization of nanomaterials, elimination of contact resistance for electronic device processing, and local metallization of material surfaces. The demonstration of microelectrode fabrication on layer nanomaterials using the FIB deposition method can serve as a crucial and useful reference for future researchers and engineers in academia and the industry.

Disclosures

The authors have nothing to disclose.

Acknowledgements

RSC thanks the support of the National Science Council (NSC) of Taiwan under Project NSC 102-2112-M-011-001-MY3. YSH acknowledges the support of the NSC of Taiwan under Project NSC 100-2112-M-011-001-MY3.

References

1. Wilson, J. A., &Yoffe, A. D. The transition metal dichalcogenides discussion and interpretation of the observed optical, electrical and structural properties. *Adv. Phys.* **18** (73), 193-335, (1969).
2. Ataca, C., Sahin, H., Ciraci, S. Stable, Single-layer MX2 transition-metal oxides and dichalcogenides in a honeycomb-like structure. *J. Phys. Chem. C.* **116** (16), 8983-8999, (2012).
3. Wang, Q. H., Kalantar-Zadeh, K., Kis, A., Coleman, J. N., Strano, M. S. Electronics and optoelectronics of two-dimensional transition metal dichalcogenides. *Nature Nanotech.* **7** (11), 699-712, (2012).
4. Mak, K. F., Lee, C., Hone, J., Shan, J., Heinz, T. F. Atomically thin MoS_2: A new direct-gap semiconductor. *Phys. Rev. Lett.* **105** (13), 136805, (2010).
5. Splendiani, A., *et al.* Emerging photoluminescence in monolayer MoS_2. *Nano Lett.* **10** (4), 1271-1275, (2010).
6. Lebègue, S., & Eriksson, O. Electronic structure of two-dimensional crystals from *ab initio.* theory. *Phys. Rev. B.* **79** (11), 115409, (2009).
7. Kuc, A., Zibouche, N., Heine. T. Influence of quantum confinement on the electronic structure of the transition metal sulfide *T*.S_2. *Phys. Rev. B.* **83** (24), 245213, (2011).
8. Yoffe, A. D. Layer compounds. *Annu. Rev. Mater. Sci.* **3**, 147-170, (1993).
9. Chen, Y., *et al.* Tunable band gap photoluminescence from atomically thin transition-metal dichalcogenide alloys. *ACS Nano.* **7** (5), 4610-4616, (2013).
10. Radisavljevic, B., & Kis, A. Mobility engineering and a metal-insulator transition in monolayer MoS_2. *Nature Mater.* **12** (9), 815-820, (2013).
11. Zhang, Y., Ye, J., Matsuhashi, Y., Iwasa, Y. Ambipolar MoS_2 thin flake transistors. *Nano Lett.* **12** (3), 1136-1140, (2012).
12. Liu, H., Neal, A. T., Ye, P. D. Channel length scaling of MoS_2 MOSFETs. *ACS Nano.* **6** (10), 8563-8569, (2012).
13. Ghatak, S., Pal, A. N., Ghosh, A. Nature of electronic states in atomically thin MoS_2 field-effect transistors. *ACS Nano.* **5** (10), 7707-7712, (2011).
14. Ong, Z. Y., & Fischetti, M. V. Mobility enhancement and temperature dependence in top-gated single-layer MoS_2. *Phys. Rev. B.* **88** (16), 165316, (2013).
15. Hwang, W. S., *et al.* Comparative study of chemically synthesized and exfoliated multilayer MoS_2 field-effect transistors. *Appl. Phys. Lett.* **102** (4), 043116, (2013).

16. Park, W., *et al.* Oxygen environmental and passivation effects on molybdenum disulfide field effect transistors. *Nanotechnology.* **24** (9), 095202, (2013).
17. Wu, W., *et al.* High mobility and high on/off ratio field-effect transistors based on chemical vapor deposited single-crystal MoS_2 grains. *Appl. Phys. Lett.* **102** (14), 142106, (2013).
18. Larentis, S., Fallahazad, B., Tutuc, E. Field-effect transistors and intrinsic mobility in ultra-thin $MoSe_2$ layers. *Appl. Phys. Lett.* **101** (22), 223104, (2012).
19. Bolotin, K. I., *et al.* Ultrahigh electron mobility in suspended graphene. *Solid State Commun.* **146** (9), 351-355, (2008).
20. Novoselov, K. S., *et al.* Two-dimensional gas of massless Dirac fermions in graphene. *Nature.* **438** (7065), 197-200, (2005).
21. Zhang, Y., Tan, Y. W., Stormer, H. L., Kim, P. Experimental observation of the quantum Hall effect and Berry's phase in graphene. *Nature.* **438** (7065), 201-204, (2005).
22. Radisavljevic, B., Radenovic, A., Brivio, J., Giacometti, V., Kis, A. Single-layer MoS_2 transistors. *Nature Nanotech.* **6** (3), 147-150, (2011).
23. Chang, C. Y., *et al.* Electrical transport properties of single GaN and InN nanowires. *J. Electro. Mater.* **35** (4) 738-743, (2006).
24. Calarco, R., *et al.* Size-dependent photoconductivity in MBE-grown GaN-nanowires. *Nano. Lett.* **5** (5) 981-984, (2005).
25. Soci, C., *et al.* ZnO nanowire UV photodectors with high internal gain. *Nano Lett.* **7** (4), 1003-1009, (2007).
26. Nam, D. Tham, and J. E. Fischer, Disorder effects in focused-ion-beam-deposited Pt contacts on GaN nanowires. *Nano Lett.* **5** (10), 2029-2033, (2005).
27. Chen, R. S., *et al.* Anomalous quantum efficiency for photoconduction and its power dependence in metal oxide semiconductor nanowires. *Nanoscale.* **5** (15) **,** 6867-73, (2013).
28. Chen, R.S., Tang, C.C., Shen, W.C., Huang, Y.S., Thickness-dependent electrical conductivities and ohmic contacts in transition metal dichalcogenides multilayers. *Nanotechnology.* **25** (41), 415706, (2014).
29. Huang, Y. H., Peng, C. C., Chen, R. S., Huang, Y. S., Ho, C. H.,Transport properties in semiconducting NbS_2 nanoflakes. *Appl. Phys. Lett.* **105** (9), 093106, (2014).
30. Hu, S. Y., Liang, C. H., Tiong, K. K., Lee, Y. C., Huang, Y. S. Preparation and characterization of large niobium-doped $MoSe_2$ single crystals. *J. Crystal Growth.*285 (3), 408-414, (2005).
31. Das, S. and Appenzeller, J., Where does the current flow in two-dimensional layered systems?. *Nano Lett.* 13 (7), 3396-3402, (2013).
32. Cullity, B. D. *Elements of X-ray Diffraction.* 2nd edition. ISBN 0-201-01174-3, Addison-Wesley Publishing Company, Inc., Boston, Massachusetts, (1978).
33. Jadczak, J., *et al.* Composition dependent lattice dynamics in $MoS_xSe_{(2-x)}$ alloys. *J. Appl. Phys.* **116** (19), 193505, (2014).
34. Weber, W. H., Merlin R. (Eds.) *Raman Scattering in Materials Science.* ISBN 3-540-67223-0, Springer-Verlag, Berlin, (2000).
35. Tonndorf, P., *et al.* Photoluminescence emission and Raman response of monolayer MoS_2, $MoSe_2$, and WSe_2. *Opt. Express.* **21** (4), 4908-4916, (2013).
36. Hu, S. Y., Liang, C. H., Tiong, K. K., Lee, Y. C., Huang, Y. S. Preparation and characterization of large niobium-doped $MoSe_2$ single crystals. *J. Crystal Growth.* **285** (3), 408-414, (2005).
37. Hu, S. Y., Liang, C. H., Tiong, K. K., Huang, Y. S. Effect of Re dopant on the electrical and optical properties of $MoSe_2$ single crystals. *J. Alloys Compounds.* **442** (1-2), 249-251, (2007).
38. Bougouma, M., *et al.* Growth and characterization of large, high quality $MoSe_2$ single crystals. *J. Crystal Growth.* **363**, 122-127, (2013).

